High temperature high strength austenitic steel fabricated by laser powder-bed fusion

Sebastien Dryepondt, Peeyush Nandwana, Kinga A. Unocic, Rangasayee Kannan, Patxi Fernandez Zelaia, Fred A. List III

Materials Science and Technology Division, Oak Ridge National Laboratory,Oak Ridge, TN, 37831, United States

Abstract

Extremely fast cooling rates during laser powder-bed fusion (LPBF) can result in materials with unique microstructures. For LPBF 316L stainless steel, the formation of sub-grain cellular structures with high dislocation density has been linked to superior tensile properties at room temperature. This cellular structure offers also a new route for the development of high temperature LPBF steels with the nucleation of nano-size strengthening carbides in the cell walls. HK30Nb steel (Fe-25Cr-20Ni-Nb-C) was, therefore, fabricated by LPBF to evaluate its potential for high temperature applications. Optimization of the fabrication parameters yielded material with density greater than 99.7%, with nano Nb-rich precipitates in the cell walls. Annealing at 800 °C for 5h resulted in the nucleation and growth of additional precipitates mainly in the cell walls and at grain boundaries. The high dislocation density led to yield strength at 20-900 °C two to three times higher than yield strength for cast HK30Nb and the nano carbides in the cell walls significantly improved the cellular structure stability at 800 °C.

Keywords: Laser powder bed fusion (LPBF), Austenitic steel, Nano carbides, HK30Nb, tensile, cellular structure

1. Introduction

The fabrication and characterization of 316L steel by laser powder-bed fusion (LPBF) has attracted a lot of attention due to unique microstructural features leading to great room temperature tensile properties [1, 2, 3, 4, 5, 6, 7, 8, 9, 10]. Of particular significance is the presence of cellular structures with high dislocation density [11]. Dislocation in the sub cellular structure enhances the alloy yield strength while interactions between deformation twins and dislocations in the cell walls result in superior room temperature ductility [3, 4, 5, 8, 9, 12]. Recent work revealed, however, that the tensile properties of the LPBF 316L stainless steels at 400-700 °C are only moderately better than the properties of wrought 316L [13]. The main reason is a change of deformation mechanisms at T >200 °C, also observed for wrought 316L, from twinning at low temperature to dislocation motion at higher temperatures [14, 15]. Dynamic strain aging with strong interaction between solute atoms and moving dislocations is also known to reduce 316L ductility at 500-700 °C [16, 17, 18]. In addition, the stability of the cells was found to be limited at temperature above 600°C, from a significant decrease of dislocation density to a complete disappearance of the cell structure at T >800-900°C after annealing from 15min to 4h [7, 13, 19]. One promising way to stabilize the microstructure and increase the alloy strength at high temperature is to nucleate precipitates in the cell walls to pin dislocations. Several authors have shown, indeed, that for 316L fabricated by LPBF, chemical segregation of Mo and Cr and (Si,O)-rich precipitates were observed in the cell walls [1, 4, 20], leading to consider chemical segregation and nano precipitates as viable solutions for higher strength stainless steels [3, 11]. Almangour et al. [21, 22] laser melted 316L powder with either TiC or TiB2 powder and showed a significant improvement of the yield strength in compression at both room temperature and 650 °C compared to a reference LPBF 316L steel. Strengthening of the steel was attributed to a refinement of the grain structure, a refinement of the cellular structure and/or chemical segregation in the cell walls. At high temperatures, a decrease of dynamic recovery and recrystallization due to the presence of fine precipitates was also

postulated. Zhong et al. mixed 316L powder with nano Y_2O_3 powder before melting to fabricate an oxide dispersion strengthened (ODS) 316L steel. They observed the formation of (Y,Si,O) nano oxides but the impact on the LPBF 316L steel tensile properties was limited [23]. Another route for the design of high temperature high strength LPBF austenitic steels is to take advantage of the high dislocation density in the cell walls to nucleate fine carbides or carbonitrides as observed in advanced 310 or 347-type austenitic steels [24, 25, 26]. In this work we will describe the fabrication by LPBF and characterization of 310-type cast HK30Nb steel. The alloy was selected due to its use in the automotive industry for turbocharger manifold and housing [27], good castability and for its high C, Cr and Nb concentration to form NbC and $M_{23}C_6$ precipitates [28].

2. Experimental Procedure

2.1. Alloy fabrication

The HK30Nb powder, with a particle size of 15-45 μm, was purchased from Powder Alloy Corporation in two separate batches. As can be seen in Table 1, the powder chemical composition from the two gas atomization runs and the composition of the resulting LPBF alloy were very similar. The LPBF deposited part chemistry was consistent with the ASTM A297 specification except for a relatively low C. The 0.2 wt % Mn concentration was below the 2 wt % maximum specified in ASTM A297 but this value was lower than typically reported for cast HK30Nb [27]. The LPBF HK30Nb builds fabricated using a Renishaw AM250 are shown in Figure 1. Small rectangular cubes and thin walls were first fabricated to determine the optimum fabrication parameters (Figure 1a). A design of experiments was implemented to correlate the alloy density with the volumetric heat input (VHI). The power was set to 200 W, the layer thickness to 30 μm and the hatch spacing, point distance and exposure time was varied to obtain a range of VHI from 45 to 220 J/mm^3. A plot of the cube density measured by gas pycnometry versus the VHI is shown in Figure 2a. A plateau was observed with a maximum density of 7.83 g/cm^3 for VHI values between 70 and 110 J/mm^3. Based on these results, the following parameters were used to fabricate the cylindrical rods, rectangular blocks and thin plates shown in Figure 1b: hatch spacing =125 μm, exposure = 135 ms and point distance =103 μm. Later on, the LPBF HK30Nb cubes were sectioned and examples of cross-sections are shown in Figure 2b and 2c. Density measurement by image analysis using

both a Python code and ImageJ confirmed that a surface fraction density superior to 99.7% was observed for VHI values between 70 and 110 J/mm^3.

HK30Nb	**Fe**	**Cr**	**Ni**	**Si**	**Nb**	**C**	**Mo**	**Mn**
Powder1	Bal.	25	21	1.1	1.32	0.22	0.3	0.2
Powder2	Bal.	25	20	1	1.25	0.21	0.3	0.2
LPBF alloy	50.66	25.36	20.53	1.14	1.37	0.2	0.27	0.2

Table 1: Chemical composition in wt% of the HK30Nb powders provided by the powder manufacturer and the LPBF alloy measured by inductively coupled plasma (ICP), combustion, and inert gas fusion (IGF)

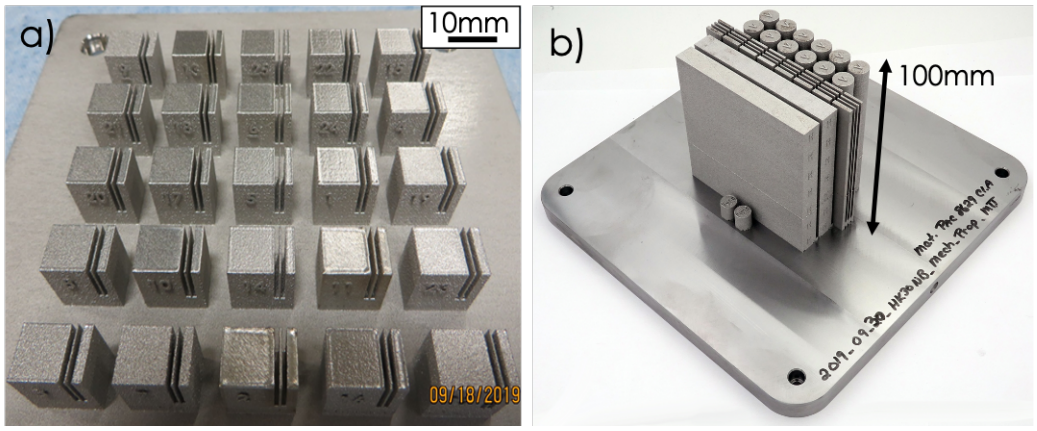

Figure 1: LPBF HK30Nb builds using a Renishaw AM250, a) Cubes and thin walls for parameter optimization, b) Cylindrical rods and rectangular bars for microstructure characterization and mechanical testing

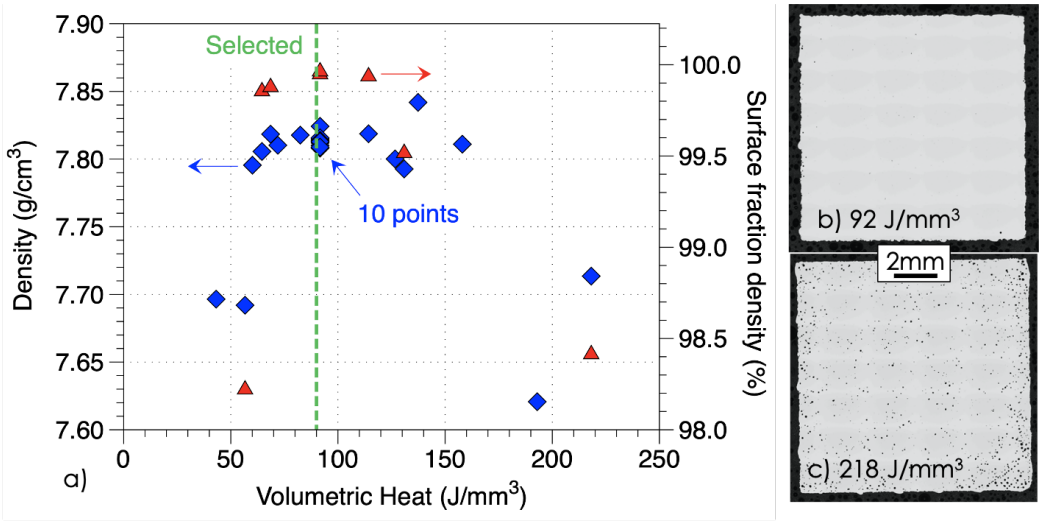

Figure 2: a) LPBF HK30Nb cube density measured by gas pycnometry or image analysis versus the volumetric heat input, b) and c) Example of cube cross-sections used to measure the surface fraction density

2.2. Tensile testing

Subsize SS3-type tensile specimens [29] with a gauge section of 2x2 mm^2 and a gauge length of 7.62 mm were machined along the build direction from the top or center of the cylindrical rods and perpendicular to the build direction from the top of one rectangular block. In both cases, the top 5mm of the build was discarded as the microstructure is expected to change in the final build layers due to variation in thermal profiles. Tensile testing was conducted at 20-900°C on an Instron electro-mechanical machine equipped with a three zone radiation furnace and the cross-head displacement was controlled to achieve a strain rate of $10^{-3}\,s^{-1}$. The gauge section was too small to insert an extensometer so the uniform and total plastic elongations were estimated from the cross head displacement curve. Three thermocouples spot welded on the specimen grips ensured control of the temperature within ±2°C. Tests were also conducted at room temperature and at 700°C using standard size threaded cylindrical specimens with a gauge length of 32 mm and a gauge diameter of 6.3mm. An MTS 632.11B-20 extensometer equipped with ceramic extension rods was used to measure the specimen deformation and three thermocouples were attached on the top, middle and bottom of the gauge length to control the temperature over the specimens within 3°C. Testing was conducted according to ASTM E21 with an initial strain rate

of $10^{-4}\,s^{-1}$ and an increase to $8.10^{-4}\,s^{-1}$ past the yield strength. Both the SS3-type and standard specimens were maintained at temperature for 30 min before testing.

2.3. Microstructure characterization

Standard metallographic techniques were used to mount samples of the as fabricated and annealed LPBF HK30Nb steel along and perpendicular to the build direction. Samples were extracted in the vicinity of the rod center in each case. For the as printed material, a second section from the top portion of another rod was also mounted to verify material homogeneity. Annealing of the LPBF HK30Nb rod was conducted for 5h at 800°C in flowing Ar followed by natural cooling in air outside the furnace. Tensile specimens tested at 20ºC, 600ºC, 700ºC and 800ºC were also characterized after rupture in different locations from the necking zone to the shoulder. Grain texture was evaluated using a Zeiss Crossbeam 550 field emission scanning electron microscope equipped with an Oxford electron backscattered diffraction (EBSD) detector. To reveal the cellular structure, some samples were electrolytically etched with a solution containing 10% oxalic acid and then imaged using an Hitachi S4800 scanning electron microscope (SEM) equipped with a cold field emission gun. Measurement of the cell size from random cellular colonies along and perpendicular to the build direction was conducted using these SEM images and the intersect method for a total of 115 measurements. For elongated cells, only the width of the cell was estimated. Scanning transmission electron microscopy (STEM) imaging and energy dispersive x-ray spectroscopy of HK30Nb were conducted on a FEI Talos F200X S/TEM operated at 200kV and equipped with an extreme field emission gun (X-FEG) electron source, high-angle annular dark-field (HAADF) detector and Super-X energy dispersive X-ray spectroscopy (EDS) system with 4 silicon-drift detectors (SDD). TEM specimens were prepared by following standard thinning/polishing procedure for TEM sample preparations of 3 mm in diameter discs. Afterwards, pre-thinned 100 μm thick 3 mm discs were electropolished using A3 Struers solution (600ml Methanol, 360ml 2- Butoxyethanol, 60ml Perchloric Acid) at -20 °C. As for the samples prepared by standard metallography, samples were extracted from the center of the rods.

2.4. Thermodynamic calculations

All the thermodynamic calculations were performed using TCFE9 database of ThermoCalc. Kinetic calculations to capture the precipitation evolution

with temperature and time were carried out with PRISMA, precipitation simulation tool working in conjunction with thermodynamic database TCFE9 and mobility database MOBFE4.

3. Results

3.1. LPBF HK30Nb Microstructure

As can be seen in Figure 3, pole and inverse pole figures of the LPBF HK30Nb steel along and perpendicular to the build direction showed no significant texture for the austenitic matrix with grains exhibiting the chevron-type shape often observed in LPBF alloys. The grain aspect ratio was 2-2.6:1 with the grain size ranging from 1 to 90 μm. A large number of small grains were detected leading to an overall grain size average of 10-12 μm. Etched optical images (Figure 4a) revealed that the main defects were lack of fusion voids at melt pool boundaries. In addition, SEM micrographs with (Figure 4b) or without (Figure 4c) etching highlighted the presence of the cellular structures reported for various alloys fabricated by LPBF, and in particular 316L steel. [3, 4, 5, 8, 9, 11, 13, 30, 31, 32]. Both elongated and "equiaxed" cells were observed but there is a growing consensus that all the cells are in fact more or less elongated, their appearance being dependent on the cross sectional plan [11]. Measured cell sizes for both the equiaxed and elongated cells (width) along and perpendicular to the build direction are summarized in Table 2. Results were very similar for the equiaxed and elongated cells in both directions, with average cell size varying from 0.52 to 0.56 μm. Measurements in random locations led to 16 measurements for equiaxed cells versus 48 for the width of the elongated cells along the build direction, while these numbers were 42 versus 20, respectively, perpendicular to the build direction. Quantitative estimate of the cell orientation is beyond the scope of this paper, but clearly a much higher ratio of elongated cells was observed along the build direction. The Cr map (representative of all elemental maps) in Figure 4d corresponds to the SEM micrograph in Figure 4c and highlights the absence of chemical segregation or precipitates easily detectable by EDS.

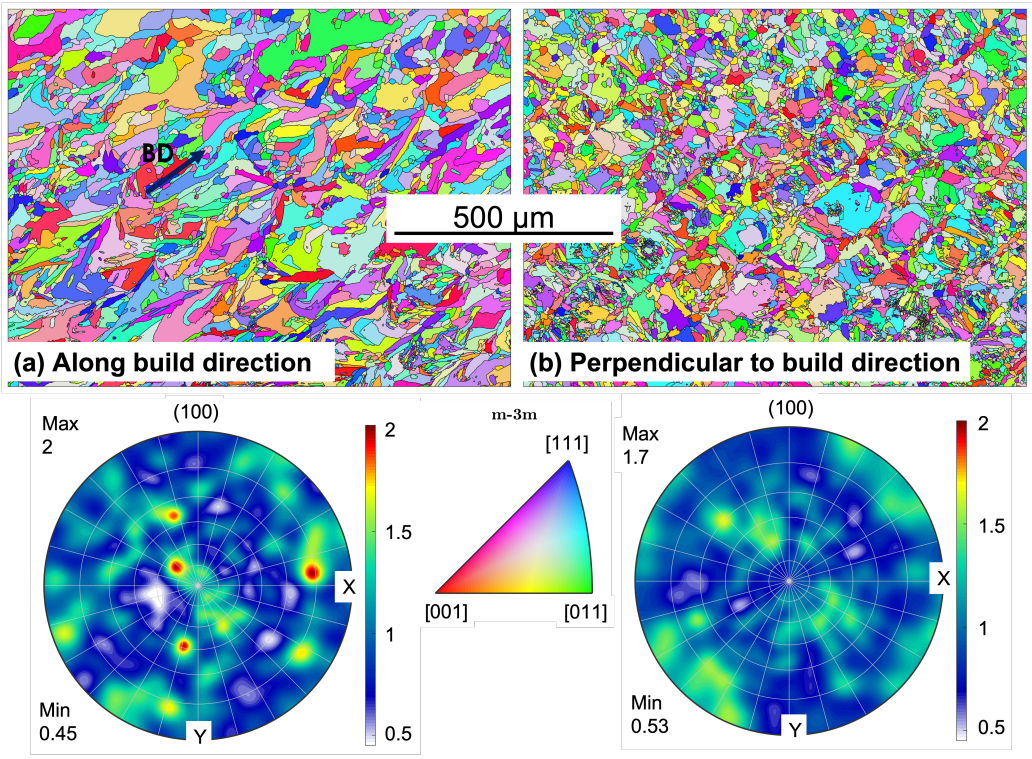

Figure 3: Inverse pole figure (IPF) maps and corresponding {001} pole figure for the as-printed LPBF HK30Nb rod, a) Along the build direction, b) Perpendicular to the build direction

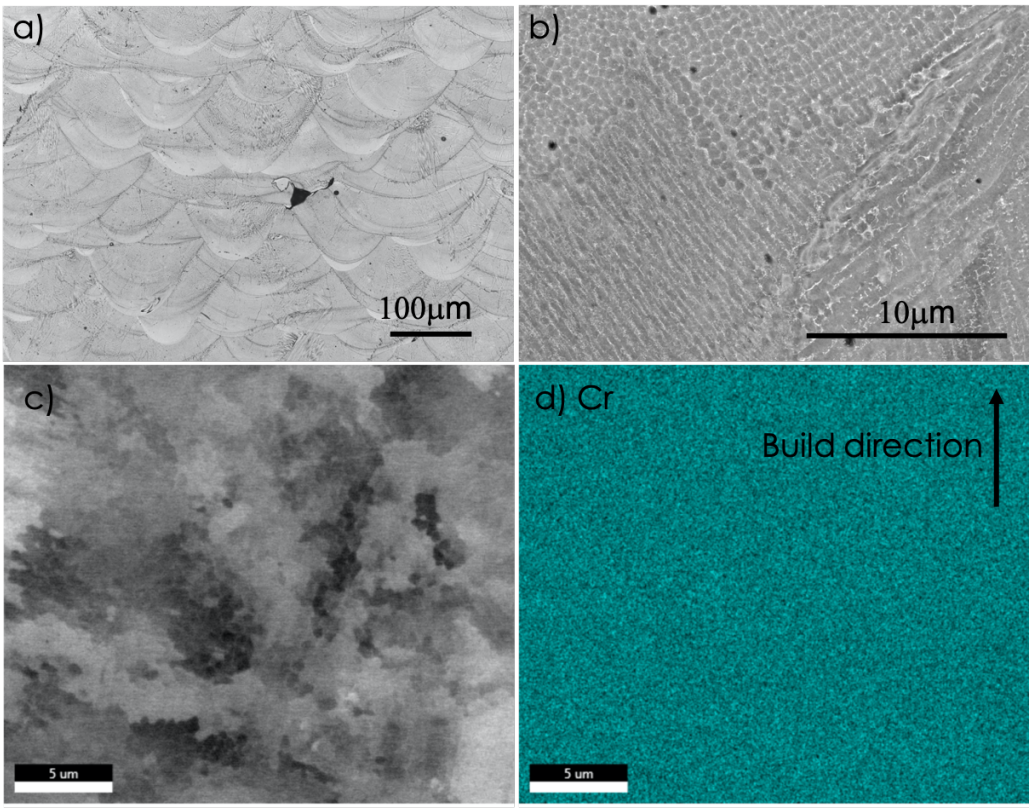

Figure 4: As printed LPBF HK30Nb along the build direction, a) Etched optical micrograph showing lack of fusion at melt pool boundaries, b) Etched BSE-SEM micrograph highlighting equiaxed and elongated cellular structures, c) BSE-SEM micrograph showing a similar cellular structure, d) corresponding EDS Cr map

The TEM images shown in Figure 5a and 5b confirmed the presence of 0.55 μm cellular structure, with a high dislocation density in the cell walls. The Nb and Cr chemical maps (Figure 5c) revealed the presence of fine Nb-rich carbides as well as Cr segregation and/or Cr-rich precipitates in the cell walls. Figure 5d also highlights the presence of small elongated Nb-rich carbides at grain boundaries. A few Cr-rich and Al-rich oxides were also observed at grain boundaries or inside grains, respectively.

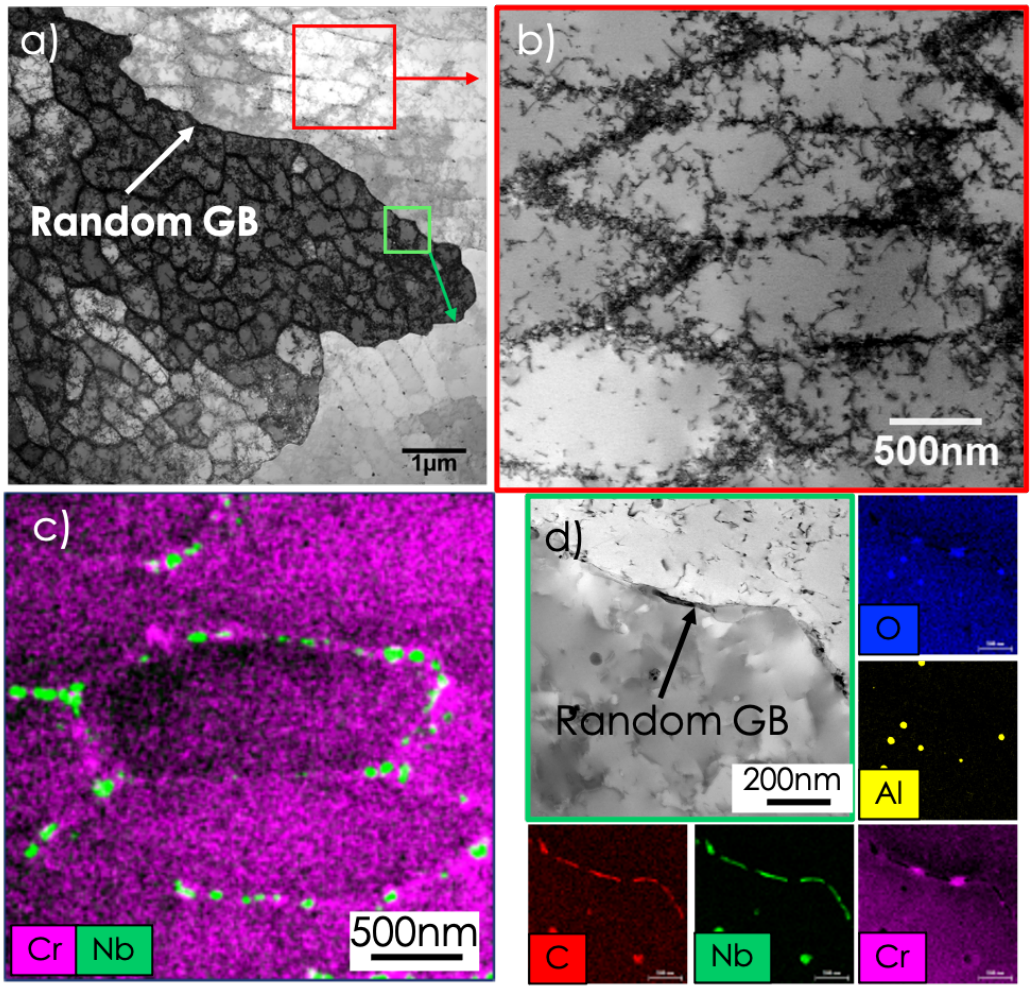

Figure 5: a) BF-STEM image of as-printed LPBF HK30Nb rod, b) and c) higher magnification BF-STEM images of the cellular structure with corresponding EDS elemental maps of Nb and Cr and d) higher magnification BF-STEM images of a random grain boundary with corresponding EDS elemental maps of C, Nb, O, Al and Cr

3.2. Tensile Properties

The tensile properties of the LPBF HK30Nb along the build direction for the SS3 and standard-size specimens are compared in Figure 6 with the tensile properties generated perpendicular to the build direction with SS3 specimens. The tensile curve examples presented in Figure 6a show that the key difference between the SS3 and standard specimens lies on the erroneous elastic portion of the SS3 curves due to the compliance of the tensile

machine. This is the reason why uniform and total plastic elongations are reported here. In addition, the arrow in Figure 6a highlights that serrated tensile curves were observed at 600°C, indicating that dynamic strain aging took place. At T < 600°C, the yield strength and UTS of the LPBF HK30Nb steel perpendicular to the build direction were slightly higher than the yield stress and UTS in the longitudinal direction, with a more significant difference for the yield stress at room temperature. Both the yield strength and UTS values were comparable at T > 700°C. In both directions, the total plastic deformation decreased progressively with increasing temperature, and the ductility was higher at all temperatures perpendicular to the build direction. The uniform elongation remained the same at 20-400°C, decreased slightly at 600°C and then drastically decreased at T>700°C. Data generated at 20°C and 700°C with standard specimens were very consistent with the results generated on small SS3-type dog bone specimens except for the lower ductility at 700°C. Lower ductility for standard specimens in comparison with SS3-type specimens were previously reported by Dryepondt et al. [13] for 316L fabricated by LPBF. Gussev et al.[29] studied in details the effect of scale factor on tensile testing and attributed higher ductility for SS3-type specimens to a change of stress state in the necking zone.

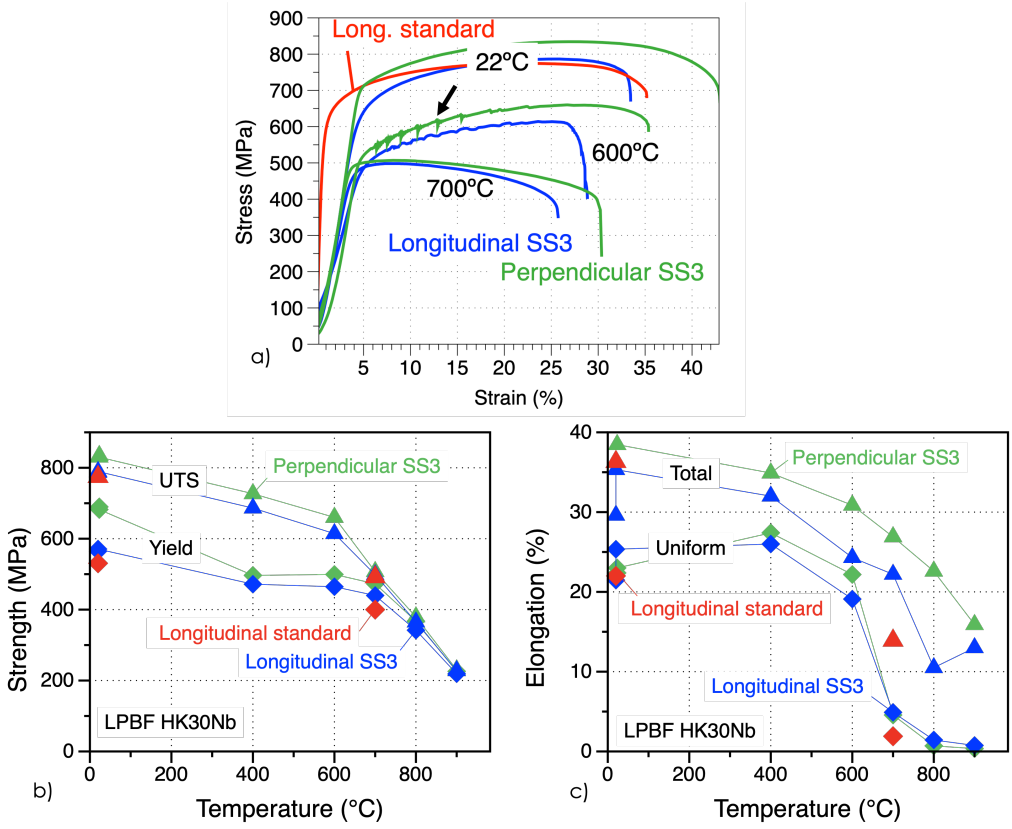

Figure 6: Tensile properties of LPBF HK30Nb along and perpendicular to the build direction, a) Examples of tensile curves at 22°C, 600 °C, 700 °C. Black arrow highlights serrated curves at 600 °C b) Yield and ultimate tensile strength, c) Uniform and total elongation. Two tests were conducted at room temperature along the build direction

The tensile properties of the LPBF HK30Nb steel along the build direction are compared in Figure 7 with the tensile properties of cast HK30Nb [33, 34], wrought 310 [35, 36] and wrought 310HCbN/HR3C [37, 38]. Grain sizes were estimated to be 70-75 μm for the HK30Nb, 100 μm and 25 μm for the 310 in the Shi et al. and VanEcho et al. studies, respectively, and 50-60 μm for the 310HCbN. The yield strength values for the cast HK30Nb and wrought 310-type steels were significantly lower compared to the yield values for LPBF HK30Nb at 20-900°C, with notable variations between the wrought 310 data reported by Shi et al. and VanEcho et al.[35, 36]. The UTS of the LPBF HK30Nb steel was also superior to the UTS of HK30Nb and 310 steels at all temperatures. Finally, the wrought 310-type steels ex-

hibited superior ductility with elongation at rupture varying from 35% to 75% . The ductility of the cast HK30Nb was similar to the ductility of the LPBF HK30Nb steel at T = 600°C and 700°C but superior at 800°C and 900°C. To further analyse the relationship between ductility and strength, the total elongation versus yield strength at room temperature for the LPBF HK30Nb steel is compared in Figure 8 with literature data for LPBF 316L [4, 20, 39] and wrought / cold rolled (WCR) 310 [35, 36, 40]. The LPBF HK30Nb data generated along the build direction at room temperature are consistent with the trend observed for WCR 310 while data generated perpendicular to the build direction matched the trends for the LPBF 316L. Finally, pole and inverse pole figures in the necking zone and head of tensile specimens tested at 20°C and 600°C are displayed in Figure 9. As reported by Dryepondt et al.[13] for LPBF 316L, deformation twins were observed in the necking zone of the specimen tested at 20°C but were not observed for the specimen tested at 600°C. It is apparent from the necking zone IPF maps as well as pole figures that at both room temperature and 600°C there are two distinct texture contributions from {001} and {111} in the tensile direction. Prior works have made similar observations in other austenitic stainless steels [41, 42]. This texture evolution is fundamentally driven by the crystal-scale plasticity which favors specific slip planes and directions for accommodating plastic deformation. Grains poorly oriented for slip will either re-orient, or if the stacking fault energy is sufficiently low, accommodate deformation via deformation twins [42]. Elevated temperatures can significantly affect the resulting deformed textures as slip is a thermally activated process which may explain subtle differences between observed textures at room temperature and 600°C.

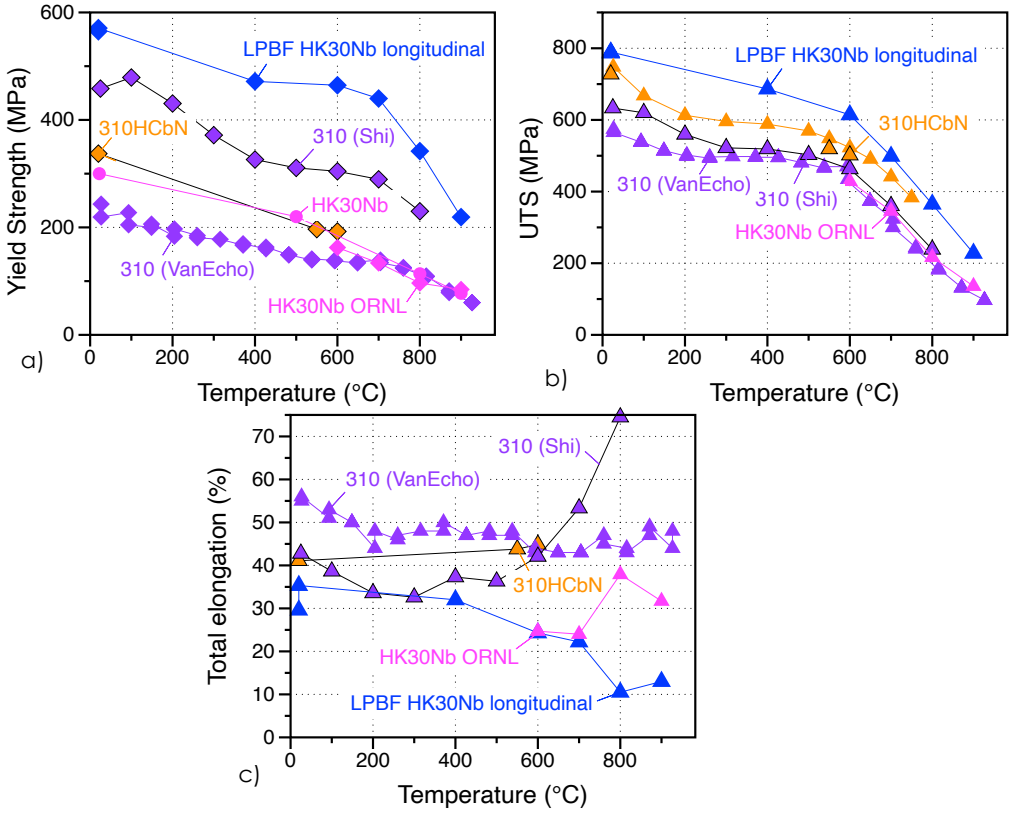

Figure 7: comparison of the tensile properties of LPBF HK30Nb, cast HK30Nb and wrought 310-type steels at 20-900°C, a) Yield and ultimate tensile strength, b) plastic deformation

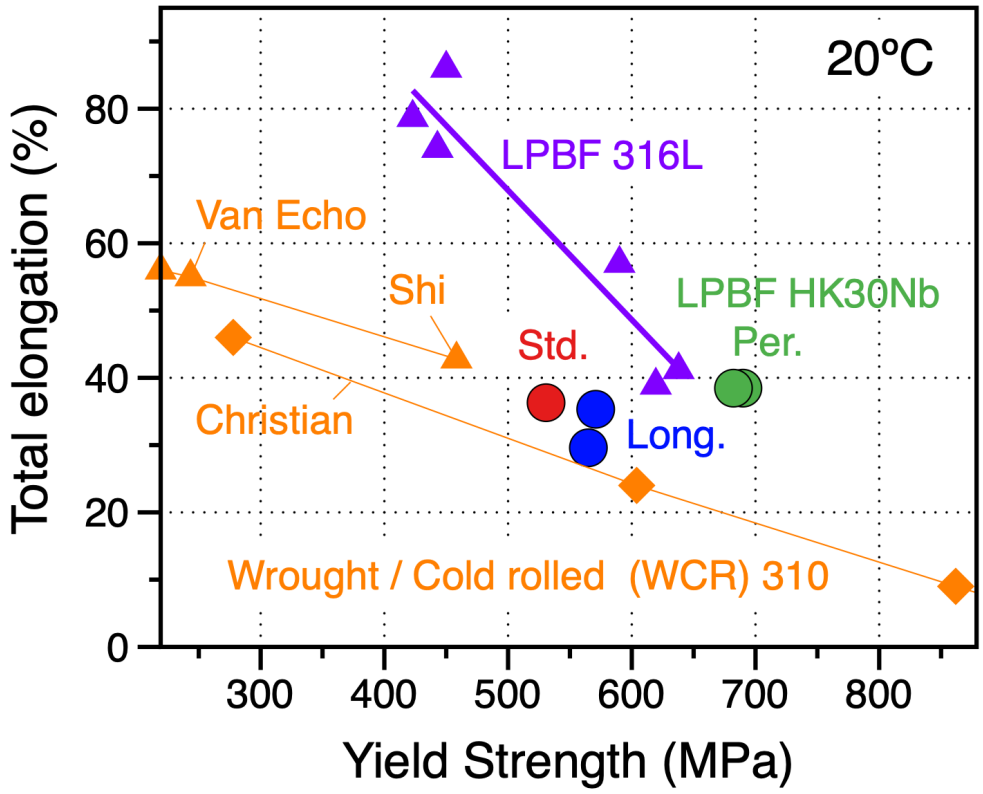

Figure 8: Comparison of the total elongation versus yield strength for the LPBF HK30Nb along (Long. and Std. for the standard size specimen) and perpendicular (Per.) to the build direction, wrought/cold rolled 310 and LPBF 316L at 20°C

3.3. LPBF HK30Nb microstructure stability

Initial assessment of the alloy microstructural and mechanical stability was conducted by annealing the LPBF HK30Nb steel for 5h at 800°C and then performing tensile testing at 20-900°C. The annealing temperature was selected because of its relevance for stress relief. Comparison of Figure 10a-10c with Figure 5a-5b highlights a similar cellular structure before and after annealing. EBSD maps (not shown) also revealed that the grain structure was unaffected by the heat treatment. The cellular structure size was estimated along the build direction to confirm that the average width of the cell, about 0.5 μm, was not affected by the 5h at 800°C anneal (Table 2). Precipitates along grain boundaries were noticed in the SEM micrographs

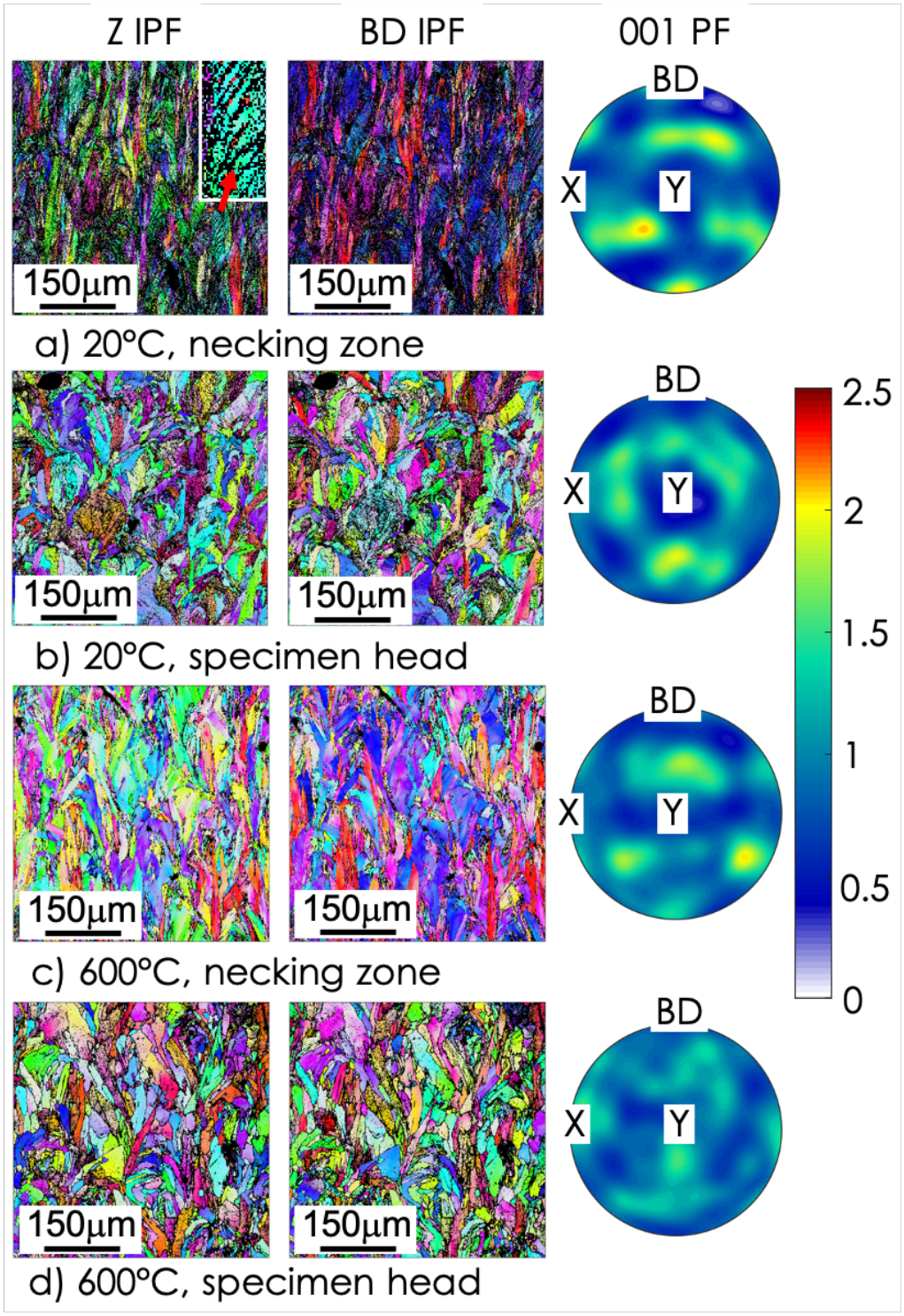

Figure 9: Inverse pole maps (left) out-of-plane sample direction (middle) vertical tensile direction and (right) 001 pole figure, a) 20 °C test, necking zone, b) 20 °C test, specimen head, c) 600 °C test, necking zone, d)600 °C test, specimen head. Insert in a) highlights the presence of deformation twins.

of Figure 10a (black arrows) and TEM characterization showed that these precipitates were either (Ni,Si)-rich, Cr-rich or Nb-rich (Figure 10d). As observed in the as fabricated steel, many Nb-rich precipitates were present in the cellular structure walls. The higher magnification STEM-EDS maps shown in Figure 11 revealed in fact various precipitates in the vicinity of the cell walls; (Fe,Cr,Ni)-rich precipitates, Cr-rich carbides and Nb-rich precipitates. Si segregation was observed but did not seem to be directly related to any of the precipitates. At even higher magnification (Figure 12), many Nb-rich carbides less than 5 nm in size could be observed in the cell interior. A precise measurement of the dislocation density by TEM was difficult due to the inhomogeneity of the cellular structure, but, comparing Figure 5b and 10b, dislocation density might be slightly reduced after 5h at 800°C.

Finally, the tensile properties along the build direction before and after annealing for 5h at 800°C were compared in Figure 13 for the LPBF HK30Nb steel and a 316L steel also fabricated by LPBF [13]. Annealing for 5h at 800°C led to a decrease of the yield strength at all temperatures for the 316L steels, while the yield strength at T<600°C was higher for the HK30Nb steel after annealing and similar before and after annealing at T>600°C. The opposite was observed for the deformation at rupture with an increase at all temperatures after annealing for the LPBF 316L and a decrease of ductility after annealing for the LPBF HK30Nb at T<600°C.

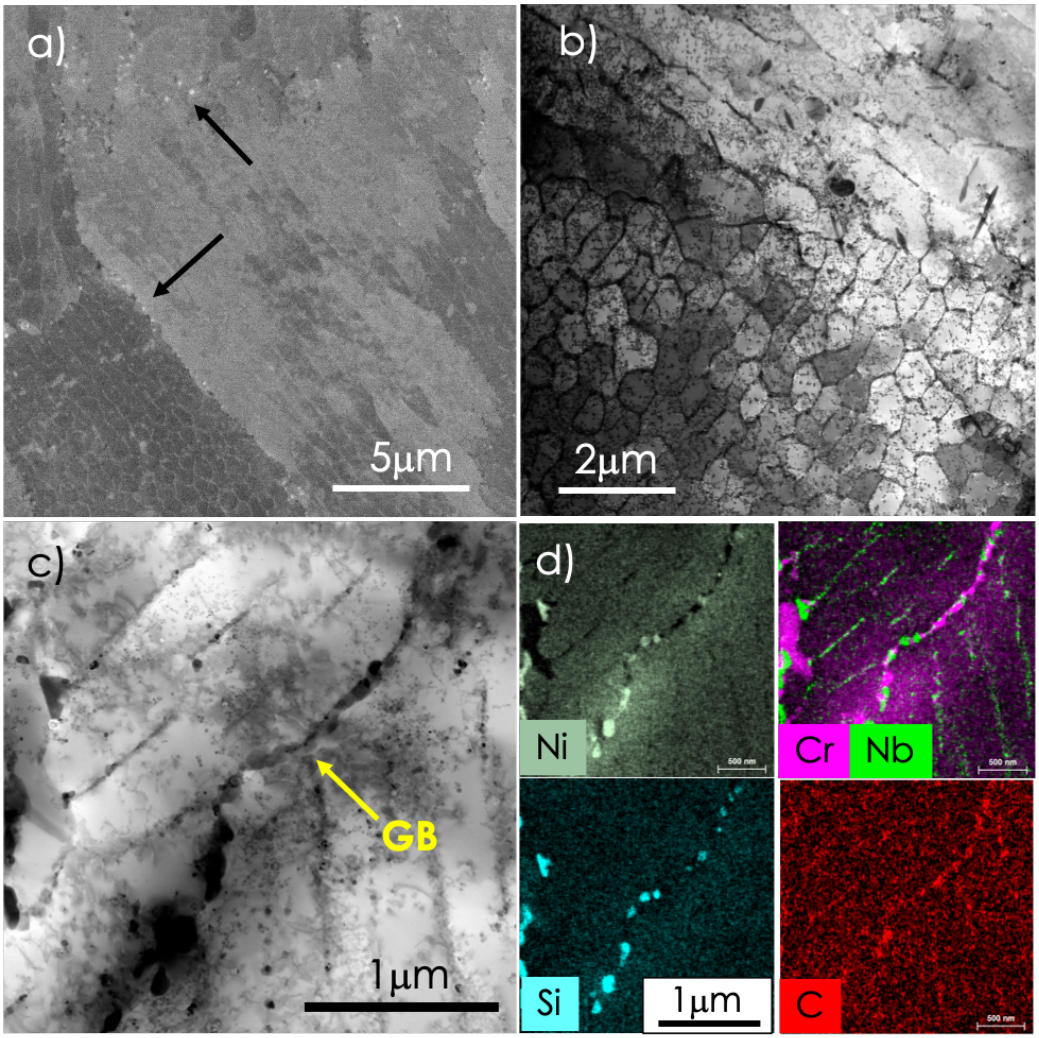

Figure 10: LPBF HK30Nb microstructure after annealing for 5h at 800°C. a) BSE-SEM image with black arrows highlighting precipitates at grain boundary. b) and c) BF-STEM images, d) EDS elemental maps of Ni, Si, Cr and Nb corresponding to Fig. 10c.

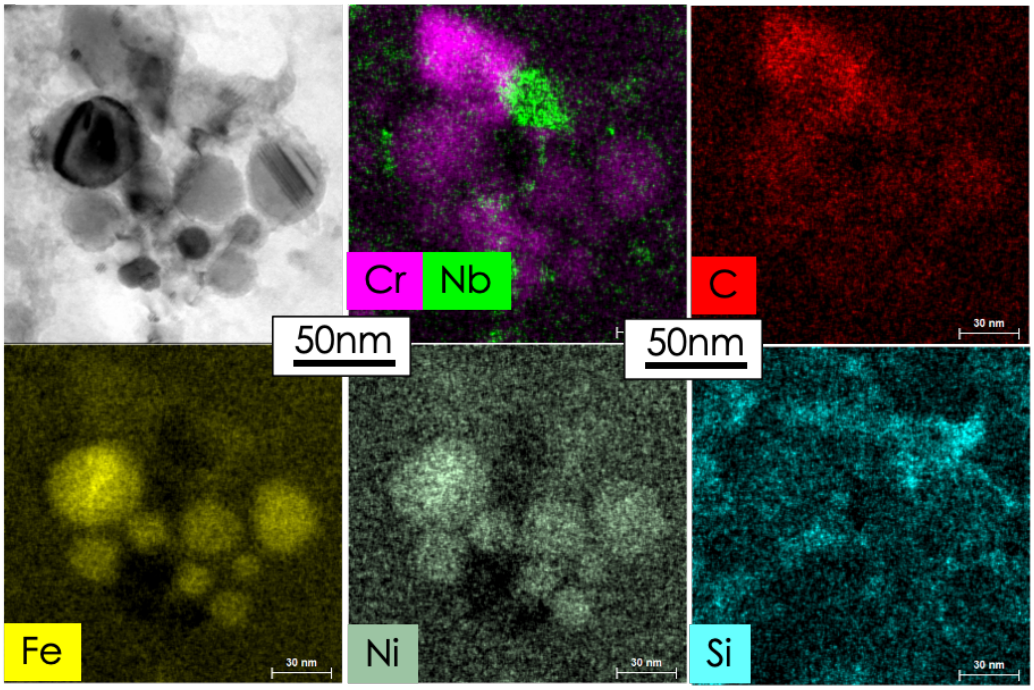

Figure 11: BF-STEM image with corresponding EDS elemental maps showing the LPBF HK30Nb microstructure in the cell wall after annealing for 5h at 800°C

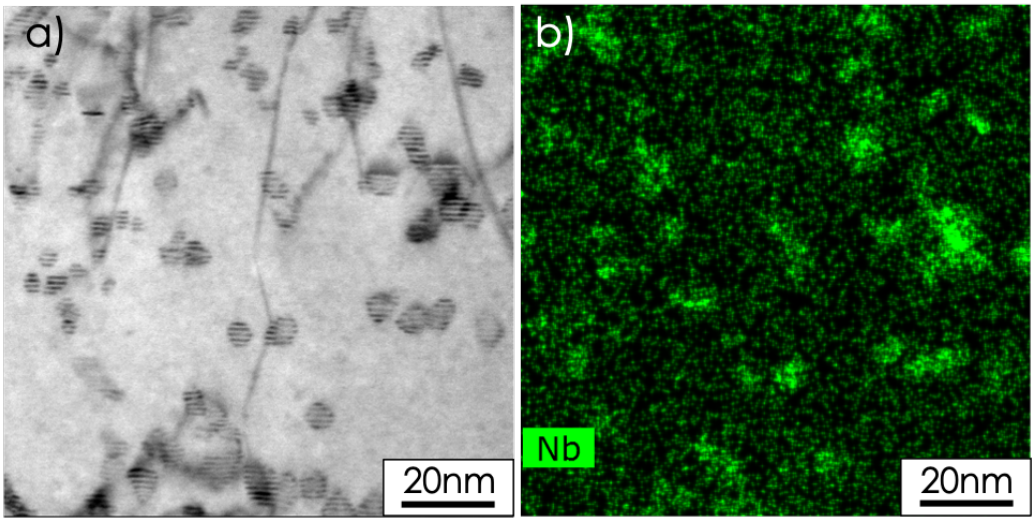

Figure 12: Nb-rich nano precipitates in the cell interior of the LPBF HK30Nb steel after annealing for 5h at 800°C, a) BF-STEM image, b) EDS Nb map

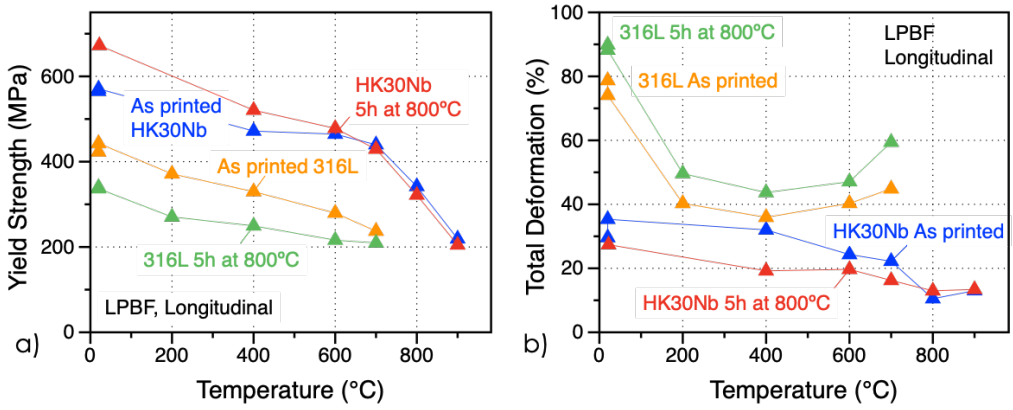

Figure 13: Comparison of the tensile properties between LPBF HK30Nb and 316L steels before and after annealing for 5h at 800°C, a) Yield strength and b) Total deformation at rupture

4. Discussion

4.1. Precipitate formation

The entire microstructure consists of inter cellular regions, cell wall regions, and grain boundaries. For a given control volume, the smaller cell

size in comparison with grain size results in a higher fraction of cell boundaries compared to grain boundaries and thus a higher fraction of nucleation sites for precipitates. The cell walls and grain boundaries can be assumed to be the last to solidify and the inter-cellular regions the first to solidify. The compositional gradients generated during solidification were, therefore, calculated using Scheil solidification simulation considering back-diffusion of solutes for the cooling rates indicative of laser powder bed fusion (10^4 K/s) using the 2020a version of ThermoCalc. Table 3 shows drastic increase in C and Nb and moderate increase in Cr, Mo and Si concentrations in the cell walls in comparison with the inter cellular regions. Precipitation simulations were conducted using thermal profiles representative of the LPBF process and tensile testing conditions (Figure 14). Rapid cooling from the solidification regime was first considered (10^4 K/s) followed by slow heating (10°C/min) up to 900°C, the maximum tensile testing temperature. Similar simulations were also conducted with the addition of a 5h anneal at 800°C step after rapid cooling. For all the precipitation simulations, a representative dislocation density of $10^{15}m^{-2}$ was chosen for the cell walls [9, 43] and the following interface energies of precipitation were used: $0.25J.m^{-2}$ for MX/austenite, $0.27J.m^{-2}$ for $M_{23}C_6$/austenite and $0.18J.m^{-2}$ for G-phase/austenite [43, 44]. A great similarity in terms of precipitates formation was predicted between the cell walls and grain boundaries, and comments below for the cell walls are applicable to grain boundaries. As can be seen in Figure 14, only MX were predicted in the cell walls in the as printed condition, and annealing at temperature above 600°C was required for the G-phase and $M_{23}C_6$ carbides to form. The predicted fractions of G-phase and $M_{23}C_6$ increased then rapidly to maximums after reaching 650°C. The fraction of $M_{23}C_6$ then plateaued while a slight decrease of the G-phase fraction was observed at higher temperature. For the inter cellular region, no precipitates were predicted after printing and a small amount of $M_{23}C_6$ was predicted to form at T>600°C. Annealing for 5h at 800°C before heating the specimens to the tensile testing temperature led to predicted precipitate fractions in the two regions similar to the maximum fractions previously predicted after ramping up to T>650°C. All these simulations are in good agreement with the observed precipitates in the as printed and 5h 800°C anneal conditions. The MX precipitates are consistent with the Nb-rich precipitates within the cell walls and grain boundaries in the as printed and annealed conditions (Figure 5 and Figure 10 to 12), and the predicted $M_{23}C_6$ and G-phase precipitates after 5h at 800°C agree with the Cr-rich carbides and the Ni or Si-rich precipitates observed, respectively

(Figures 10 and 11). A precise determination of the nature of all the precipitates present in the material before and after annealing is beyond the scope of this paper and will be the topic of a subsequent article. Although relevant to LPBF conditions, rapid cooling does not capture the full thermal profile during printing. Repetitive laser exposure will result in thermal cycling, and Sabzi et al. [45] predicted four cycles with peak temperatures of 2675 K, 2119 K, 1563 K and 1006 K. The simulations shown in Figure 14c revealed that the final volume fraction of MX precipitates was similar whether thermal cycling was considered or rapid cooling (10^4 K/s) from the solidification regime was simply assumed. Phase predictions based on rapid cooling are, therefore, relevant. In addition, previous simulations did not integrate the 30min hold time before tensile testing. As can be seen in Figure 14d for the fraction of $M_{23}C_6$ carbides, calculations were also performed considering the 30min hold time before testing at 600 °C and 900 °C to highlight the limited impact of the 30min hold time on microstructure evolution. Finally, to assess the stability of these precipitates, equilibrium phase fractions were compared in Figure 15 for the powder, cell wall, and inter cellular region using Table 1 and 3 chemical compositions. These results were also initially used to help determine the relevant phases to be considered in the previous calculations. As can be seen in Figure 15, $M_{23}C_6$ carbides and G-phase are expected to be the most stable precipitates in the cell walls, with fractions similar to what was calculated previously using PRISMA after 5h at 800°C. Small fraction of MX precipitates above 800°C and sigma phase between 700°C and 800°C were also predicted. As expected , very low fractions of precipitates were predicted in the inter cellular region, with a noticeable peak for sigma phase at 700°C. Intermediate fraction of $M_{23}C_6$ and G-phase are expected when considering the powder chemistry, but the fractions fell drastically above 700°C. A significant fraction of sigma phase is expected at temperature above 450°C with a progressive decrease as temperature increases until the phase disappears above 900°C. Interdiffusion between the cell wall and the inter cellular region will of course take place at high temperature, leading to chemical concentrations closer to the powder chemistry over time, but retardation of the sigma phase formation will likely be beneficial as will be discussed in the next section.

Region	C	Nb	Cr	Mo	Si	Mn	Ni
Cell wall	0.45	3.4	33.5	1.33	1.98	0.45	28.5
Inter-cellular	0.06	0.35	30.9	0.78	1.53	0.41	29.5

Table 3: Estimate of the chemical composition in wt% in the cell wall and inter-cellular regions using Scheil solidification simulation

4.2. Effect of LPBF microstucture on tensile strength

4.2.1. Impact of the dislocations within cell walls

Many papers on 316L steel fabricated by LPBF highlighted the strengthening effect of the cellular structure, with two key mechanisms being proposed. [4, 8, 9, 13]. Several authors simply estimated that the cellular structure resulted in a strengthening effect similar to the Hall-Petch effect for grains [4, 5]:

$$\sigma_Y = \sigma_0 + kd^{-0.5} \tag{1}$$

where d is the average grain size

On the other side, Yin et al. considered that the high dislocation density within the cell walls was key, and X-ray diffraction measurements in LPBF 316L steel were used to determine the dislocation contribution to the alloy yield strength according to equation [9]:

$$\sigma_Y = M\alpha\mu b\sqrt{\rho} \tag{2}$$

where M is the Taylor factor, α an empirical constant, μ the shear modulus, b the Burgers vector and ρ the dislocation density. It is worth noting that if we consider that all the dislocations are located in the cell walls and the dislocation density in the cell walls is independent of the cell size, then the average dislocation density in the steel will be proportional to the ratio between the surface and the volume of the cell. For a cell shape based on an hexagonal prism with the height h proportional to the base edge a, the cell volume is proportional to a^3 and the cell surface to a^2 so this ratio is inversely proportional to a. Equation 1 can therefore be approximated by:

$$\sigma_Y = M\alpha\mu bCa^{-0.5} \tag{3}$$

Again, a linear relationship between the yield strength and $a^{-0.5}$ is predicted, which could explain why a Hall Petch relationship can provide an

	Cell size in μm		
	As Printed		5h at 800°C
	Longitudinal	Perpendicular	Longitudinal
Equiaxed	0.52 ± 0.1	0.56 ± 0.07	0.45 ± 0.05
Elongated	0.53 ± 0.08	0.52 ± 0.1	0.54 ± 0.12

Table 2: Average cell size in μm along and perpendicular to the build direction in the as printed and 5h at 800°C anneal conditions. Only the width of the elongated cells was estimated.

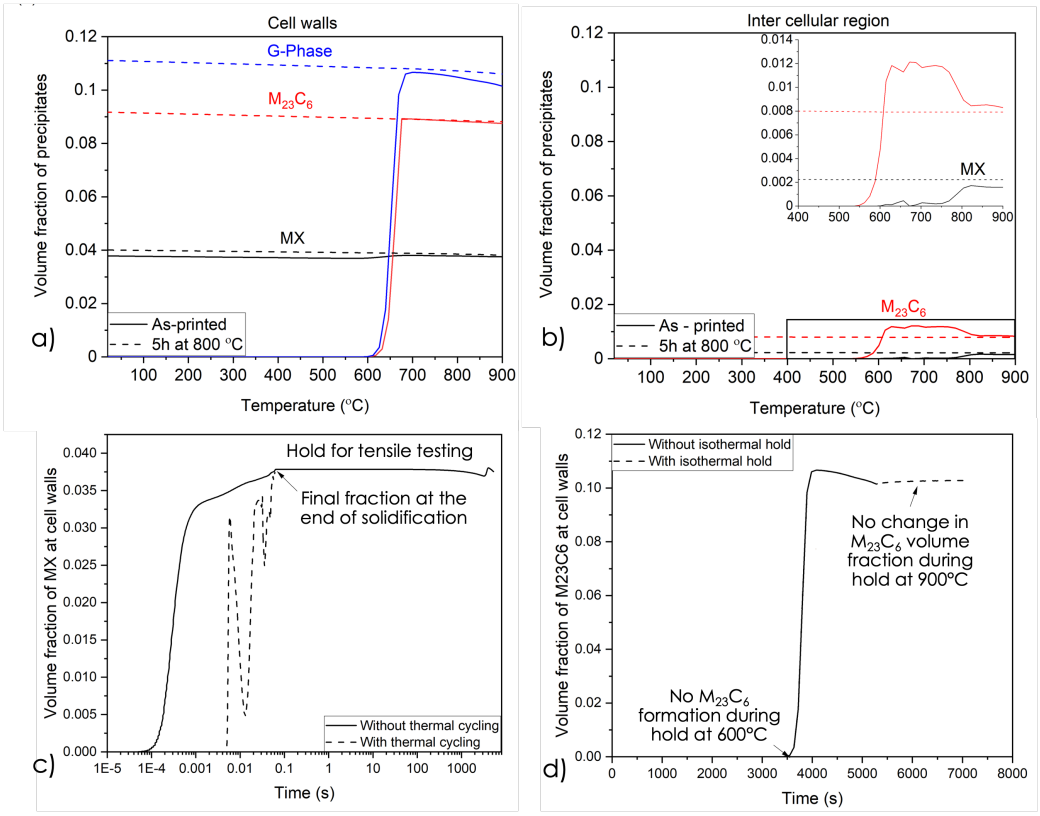

Figure 14: Precipitate evolution at a)cell walls,b) inter-cellular regions computed using PRISMA. It should be noted that G-Phase does not form in the inter-cellular regions and hence not represented in the figure. The solid line represents precipitate evolution post fabrication upon heating to tensile testing. The dotted lines represent precipitate evolution after isothermal aging at 800°C for 5 hours and heating the aged sample to tensile testing temperature. c) Volume fraction of MX precipitates considering either the thermal profile proposed by Sabzi et al. [45] or rapid cooling, d) Calculation showing the limited impact of a 30min hold time at 600 °C or 900 °C on the volume fraction of $M_{23}C_6$

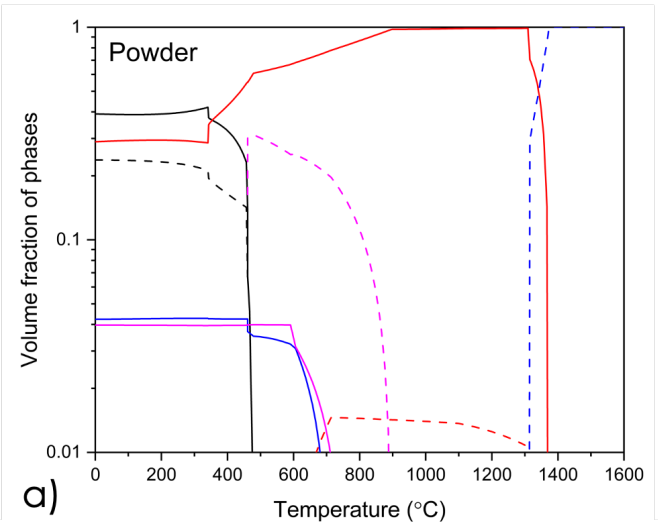

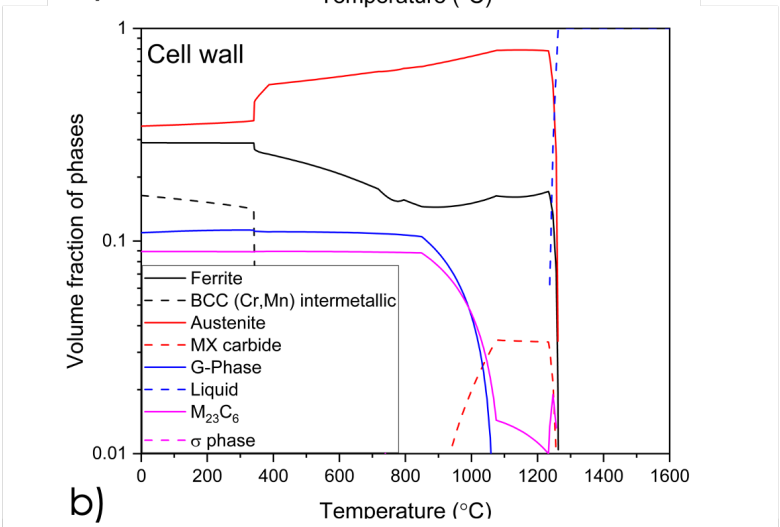

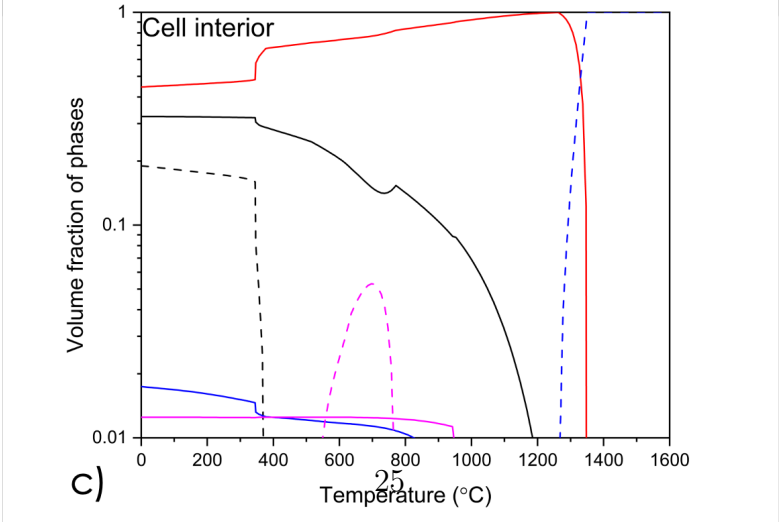

Figure 15: Equilibrium phase fraction evolution a) for the nominal powder chemistry, b) for the inter-cellular region, and c) for the intra-cellular region based on the composition summarized in Table 1 and 3. Legend is the same in a), b) and c)

adequate estimate of the LPBF 316L alloy yield strength. Wang et al. estimated σ_0 and k in equation (2) to be equal to 183 MPa and 254 MPa $\mu m^{-0.5}$, respectively, for wrought 316L based on literature data and they measured a quite similar relationship for the LPBF 316L when considering the cell size instead of the grain size. The Hall-Petch parameters have not been determined for wrought or cast 310-type steels and they should differ from the 316L parameters, in particular σ_0, since the alloy chemistry and therefore the solid solution strengthening [46], are different. As a first approximation, we used the 316L Hall Petch relationship with our cell size value of 0.53 μm, and calculated a yield strength of 532 MPa for the LPBF HK30Nb steel, compared to a measured value of 568 MPa. This result indicates that, as for LPBF 316L, the cellular structure is likely playing a key role in the high yield strength values observed for the LPBF HK30Nb steel. Significantly higher yield strength values were measured for the LPBF HK30Nb in comparison with wrought or cast 310-type steels (Figure 7) but Figure 8 shows that these yield strength values are consistent with a cold rolled 310 steel with high dislocation density. The specific chevron-like grain structure of the LPBF HK30Nb alloy with numerous small grains led to an average grain size of 10-12 μm, significantly lower value than the average grain sizes for the 310-type cast and wrought alloys, estimated to be between 25 and 100 μm. This value of 10-12 μm is still 20 times larger than the 0.5 μm average cell size, resulting in minor effect of the grain size on the tensile strength in comparison with the cellular structure impact.

4.2.2. Impact of precipitates in the cell walls

Strengthening of LPBF 316L steels due to the presence of nano precipitates, mainly SiO_2, has been proposed by a few authors [11] but others concluded that this effect was likely minimal [4, 39]. In the as printed conditions, Figure 8 shows that the yield strength at room temperature of the LPBF HK30Nb steel is similar to the yield strength of LPBF 316L steels with similar cellular structure size (0.5 μm). Assuming that the solid solution strengthening is not significantly different between LPBF 316L and HK30Nb alloys, then we can conclude that the nano Nb-rich carbides do not impact drastically the LPBF HK30Nb steel strength. In addition, Ekstrom et al.[33] reported that NbC precipitates in an HK30Nb alloy only slightly increased the yield strength of the alloy in comparison with a similar Nb-free HK30 alloy. Interestingly, the higher yield strength values observed at 20-600°C after annealing for 5h at 800°C can be attributed to the nucleation

and growth during annealing of new precipitates such as $M_{23}C_6$ and G phase precipitates. This is particularly remarkable when considering that a small decrease of the yield strength would be expected due to reduction of the dislocation density after annealing. At testing temperature > 600°C, these precipitates will form during the 30min soak time and similar yield strength values were observed before and after annealing at T > 600°C. In conclusion, the precipitates do increase the LPBF HK30Nb yield strength but this effect is quite moderate in comparison with the dislocation/cell structure effect. In addition, precipitates in the cell walls are likely to play a key role in stabilizing the cellular structure by pinning dislocations within the walls. Figure 10 shows, indeed, that the cellular structure in the LPBF HK30Nb steel was stable after annealing for 5h at 800°C contrary to what has been reported by others for LPBF 316L at 800-900°C [10, 19, 13]. The cellular structure stability at 800°C explains the similar or higher yield strength measured after annealing for 5h at 800°C when a significant decrease of the yield strength was observed for the LPBF 316L (Figure 13a). It is worth noting that dislocation pinning by fine carbides or carbonitrides is key to the creep performance of advanced 310-type or 347-type steels and the high density of carbides in the LPBF HK30Nb cell walls will likely have a positive impact on the steel creep performance [25, 26, 47]. Based on these initial high temperature tensile results, creep tests were initiated and will be reported in a subsequent publications.

4.3. Effect of LPBF HK30Nb microstructure on ductility

LPBF 316L steels have attracted remarkable attention due to the combination of high strength and high ductility at room temperature in comparison with wrought 316L [3][4][5][8][9]. Figure 8 shows, indeed, that for a given yield strength, the ductility of LPBF 316L is superior to the ductility of cold rolled wrought 316L at yield strength below 650MPa. The great ductility of the LPBF 316L steel was attributed to a strong interaction between deformation twins and dislocations in the cell walls[4, 8, 6]. Dryepondt et al. [13] showed, however, that the ductility of LPBF 316L decreased significantly at temperature above 200°C due to a change in deformation mechanisms, i.e. without deformation twins at T > 200°C. Reduction of the steel ductility was also attributed to dynamic strain aging (DSA), with serrated curves observed at 600°C. Figure 9 shows similar microstructural observations for the LPBF HK30Nb steel, with deformation twins being present in the specimen tested at room temperature but not in the specimen tested at 600°C. In addition,

a serrated tensile curve was observed at 600°C (Figure 6a) indicating that DSA is also decreasing the LPBF HK30Nb steel ductility at high temperature. Figure 8 shows that the LPBF HK30Nb ductility is consistent with the ductility of LPBF 316L with similar yield strength indicating that the initial high density of Nb-rich precipitates in the cell wall and at grain boundaries do not significantly affect the steel ductility. Of course, the presence of NbC precipitates is not the only difference between the two alloys, but Figure 7 also shows that the ductility of the Nb(C,N)-containing 310HCbN steel [26] is in the ductility range of the Nb-free 310 steels. Formation of $M_{23}C_6$ and G-phase precipitates led only to a slight reduction of the steel ductility at temperature below 600°C, but long-term annealing is required to characterize precipitate evolution and its impact on the alloy ductility. $M_{23}C_6$, sigma and G-phase precipitates have been reported to form at grain boundaries after creep testing at 750°C in an HK30Nb alloy [28] and all these phases are known to embrittle grain boundaries in 310-type steel [48, 49, 50]. Nevertheless, the cell structure in LPBF open new opportunities for alloy design with the formation of nano precipitates in the cell walls to improve the alloy high temperature mechanical properties.

5. Conclusion

An advanced austenitic steel, HK30Nb (Fe-25Cr-20Ni-Nb-C), was successfully fabricated by laser powder bed fusion. An alloy density superior to 99.7% was achieved with no cracks and a 500nm cellular structure similar to what has been reported for LPBF 316L. A key difference was the presence of nano Nb-rich carbides in the cell walls in the as printed conditions. After annealing for 5 at 800°C, various precipitates formed, mainly in the cell walls, in agreement with kinetic/thermodynamic calculations which predicted the formation of $M_{23}C_6$ and G-phase precipitates. As expected, the high dislocation density in the cell walls led to a significant increase of the steel yield and ultimate tensile strength at 20-900°C in comparison with wrought and cast 310-type steels. The high density of precipitates likely played only a moderate role in the alloy strength but helped stabilize the cellular structure up to 800 °C. Modification of the alloy chemistry to nucleate nano precipitates in the cell walls is a very promising strategy to develop unique high strength high temperature alloys.

6. Acknowledgements

The authors would like to thank K. Carver, K. Hedrick, C.S. Hawkins, T. M. Lowe and V. Cox for assistance with the experimental work, and M. Romedenne and J. Jun for reviewing the manuscript. This research was sponsored by the US Department of Energy, Office of Energy Efficiency and Renewable Energy (EERE), Vehicle Technologies Office, Propulsion Materials Program, under contract DE-AC05-00OR22725 with UT-Battelle LLC and performed in partiality at the Oak Ridge National Laboratory's Manufacturing Demonstration Facility, an Office of Energy Efficiency and Renewable Energy user facility.

References

[1] K. Saeidi, X. Gao, Y. Zhong, Z.-J. Shen, Hardened austenite steel with columnar sub-grain structure formed by laser melting, Materials Science and Engineering A 625 (2015) 221–229.

[2] R. Casati, M. Lemke, M. Vedani, Microstructure and fracture behavior of 316l austenitic stainless steel produced by selective laser melting, Journal of Materials Science and Technology 32 (2016) 738–744.

[3] Y. Zhong, M. Liu, S. Wikman, D. Cui, Z. Shen, Intragranular cellular segregation network structure strengthening 316l stainless steel prepared by selective laser melting, Journal of Nuclear Materials 470 (2016) 170–178.

[4] Y.-M. Wang, T. Voisin, J.-T. McKeown, D. Cui, Z. Shen, Intragranular cellular segregation network structure strengthening 316l stainless steel prepared by selective laser melting, journal of nuclear materials, Journal of Nuclear Materials 470 (2016) 170–178.

[5] M.-S. Pham, B. Dovgyy, P.-A. Hooper, Twinning induced plasticity in austenitic stainless steel 316l made by additive manufacturing, Materials Science and Engineering A 704 (2017) 102–111.

[6] C. Qiu, M. Al Kindi, A.-S. Aladawi, I. Al Hatmi, A comprehensive study on microstructure and tensile behaviour of selectively laser melted stainless steel, Scientific report 8:7785 (2018) 1–16.

[7] P. Krakhmalev, G. Fredriksson, K. Svensson, I. Yadroitsev, I. Yadroitsava, M. Thuvander, R. Peng, Microstructure, solidification texture, and thermal stability of 316 l stainless steel manufactured by laser powder bed fusion, Metals 8 (2018) 1–18.

[8] L. Liu, Q. Ding, Y. Zhong, J. Zou, J. Wu, Y.-L. Chiu, J. Li, Z. Zhang, Q. Yu, Z. Shen, Dislocation network in additive manufactured steel breaks strength–ductility trade-off, Materials Today 21 (2018) 354–361.

[9] Y.-J. Yin, J.-Q. Sun, J. Guo, X.-F. Kan, D.-C. Yang, Mechanism of high yield strength and yield ratio of 316 l stainless steel by additive manufacturing, Materials Science and Engineering A 744 (2019) 773–777.

[10] E. Tascioglu, Y. Karabulut, Y. Kaynak, Influence of heat treatment temperature on the microstructural, mechanical, and wear behavior of 316l stainless steel fabricated by laser powder bed additive manufacturing, The International Journal of Advanced Manufacturing Technology (2020).

[11] D. Kong, C. Dong, S. Wei, X. Ni, L. Zhang, R. Li, L. Wang, C. Man, X. Li, About metastable cellular structure in additively manufactured austenitic stainless steels, Additive Manufacturing 38 (2021) 101804.

[12] Z. Li, B. He, Q. Guo, Strengthening and hardening mechanisms of additively manufactured stainless steels: The role of cell sizes, Scripta Materialia 177 (2020) 17–21.

[13] S. Dryepondt, P. Nandwana, P. Fernandez-Zelaia, F. List, Microstructure and high temperature tensile properties of 316l fabricated by laser powder-bed fusion, Additive Manufacturing 37 (2021) 101723.

[14] N. Byun, T.S.and Hashimoto, K. Farrell, Temperature dependence of strain hardening and plastic instability behaviors in austenitic stainless steels, Acta Materialia 52 (2004) 3889–3899.

[15] X. Wu, X. Pan, J. Mabon, M. Li, J. Stubbins, The role of deformation mechanisms in flow localization of 316l stainless steel, Journal of Nuclear Materials 356 (2006) 70–77.

[16] S. Hong, S. Lee, The tensile and low-cycle fatigue behavior of cold worked 316l stainless steel: influence of dynamic strain aging, International Journal of Fatigue 26 (2004) 899–910.

[17] B.-K. Choudary, Influence of strain rate and temperature on tensile deformation and fracture behavior of type 316l(n) austenitic stainless steel, Metallurgical and Materials Transactions A 45 (2014) 303–316.

[18] S.-L. Mannan, K.-G. Samuel, P. Rodriguez, Influence of temperature and grain size on the tensile ductility of aisi 316 stainless steel, Materials Science and Engineering 68 (1984) 143–149.

[19] K. Saeidi, X. Gao, F. Lofaj, L. Kverkova, Z.-J. Shen, Transformation of austenite to duplex austenite-ferrite assembly in annealed stainless steel 316l consolidated by laser melting, Journal of Alloys and Compounds 633 (2015) 463–469.

[20] D. Kong, C. Dong, X. Ni, L. Zhang, J. Yao, C. Man, X. Cheng, L. Kui, X. Li, Mechanical properties and corrosion behavior of selective laser melted 316l stainless steel after different heat treatment processes, Journal of Materials Science and Technology 35(7) (2019) 1499–1507.

[21] B. Almangour, M.-S. Baek, D. Grzesiak, K.-A. Lee, Strengthening of stainless steel by titanium carbide addition and grain refinement during selective laser melting, Materials Science and Engineering A 712 (2018) 812–818.

[22] B. Almangour, M.-S. Baek, D. Grzesiak, K.-A. Lee, Novel tib2-reinforced 316l stainless steel nanocomposites with excellent room- and high-temperature yield strength developed by additive manufacturing, Composites Part B 156 (2019) 51–69.

[23] Y. Zhong, L. Liu, J. Zou, D. Cui, S. Z., Oxide dispersion strengthened stainless steel 316l with superior strength and ductility by selective laser melting, Materials Science and Technology 42 (2020) 97–105.

[24] T. Sourmail, Precipitation in creep resistant austenitic stainless steels, Materials Science and Technology 17 (2001) 1–14.

[25] J.-P. Shingledecker, P.-J. Maziasz, N.-D. Evans, M.-J. Pollard, Creep behavior of a new cast austenitic alloy, International Journal of Pressure Vessels and Piping 84 (2007) 21–28.

[26] S. Vujic, R. Sandstrom, C. Sommitsch, Precipitation evolution and creep strength modelling of 25cr20ninbn austenitic steel, Materials at High Temperatures 32 (2015) 607–618.

[27] D. Pierce, A. Haynes, J. Hughes, R. Graves, P. Maziasz, G. Muralidharan, A. Shyam, B. Wang, R. England, High temperature materials for heavy duty diesel engines: Historical and future trends, Progress in Materials Science 103 (2019) 109–179.

[28] C. Oberg, B. Zhu, S. Jonsson, Creep behaviour, creep damage and precipitation in the austenitic cast steel hk30 at 750c, Materials Science and Engineering A 797 (2020) 140253.

[29] M. Gussev, J. Busby, K. Field, M. Sokolov, S. Gray, Role of scale factor during tensile testing of small specimens, in: Small Specimen Test Techniques: 6th Volume, ASTM International, 2015.

[30] M.-L. Montero-Sistiaga, S. Pourbabak, J.-V. Humbeeck, D. Schryvers, K. Vanmeensel, Microstructure and mechanical properties of hastelloy x produced by hp-slm (high power selective laser melting, Journal of Materials Science and Technology 165 (2019) 107598.

[31] Y.-S. Yoo, T.-A. Book, M.-D. Sangid, J. Kacher, Identifying strain localization and dislocation processes in fatigued inconel 718 manufactured from selective laser melting, Materials Science and Engineering A 724 (2018) 444–451.

[32] M. Liu, N. Takata, A. Suzuki, M. Kobashi, Microstructural characterization of cellular alsi10mg alloy fabricated by selective laser melting, Materials and Design 157 (2018) 478–491.

[33] M. Ekström, M. Jonsson, High-temperature mechanical and fatigue properties of cast alloys intended for use in exhaust manifolds, Materials Science and Engineering A 616 (2014) 78–87.

[34] P.-J. Maziasz, M. Wilson, Crada final report for crada number nfe-08-01671 materials for advanced turbocharger designs, ORNL report TM-2014/632 (2014) 1–17.

[35] L. Shi, D.-O. Northwood, The mechanical behavior of an aisi type 310 stainless steel, Acta Materialia 43 (1994) 453–460.

[36] J.-A. VanEcho, D.-B. Roach, A.-M. Hall, Short-time tensile and long-time creep-rupture properties of the hk-40 alloy and type 310 stainless steel at temperatures to 2000 f, Basic Engineering 89 (1967) 465–478.

[37] R.-W. Swindeman, Stainless steels with improved strength for service at 760^{o}c and above, in: Proceedings of the ASME Pressure Vessels and Piping Conference, San Diego, California, 1998, pp. ORNL/CP–97555.

[38] G. Golanski, A. Zielinski, M. Sroka, J. Slania, The effect of service on microstructure and mechanical properties of hr3c heat-resistant austenitic stainless steel, Materials 13 (2020) 1297.

[39] Z. Li, T. Voisin, J.-T. McKeown, J. Ye, T. Braun, C. Kamath, W.-E. King, Y.-M. Wang, Tensile properties, strain rate sensitivity, and activation volume of additively manufactured 316l stainless steels, International Journal of Plasticity 120 (2019) 395–410.

[40] J.-L. Christian, J.-D. Gruner, L.-D. Girton, The effects of cold rolling on the mechanical properties of type 310 stainless steel at room and cryogenic temperatures, NASA report CR-54614 (1965) 1–25.

[41] J. A. Jiménez, G. Frommeyer, Analysis of the microstructure evolution during tensile testing at room temperature of high-manganese austenitic steel, Materials Characterization 61 (2010) 221–226.

[42] S. Dancette, L. Delannay, K. Renard, M. Melchior, P. Jacques, Crystal plasticity modeling of texture development and hardening in twip steels, Acta Materialia 60 (2012) 2135–2145.

[43] V. Thampy, A. Y. Fong, N. P. Calta, J. Wang, A. A. Martin, P. J. Depond, A. M. Kiss, G. Guss, Q. Xing, R. T. Ott, et al., Subsurface cooling rates and microstructural response during laser based metal additive manufacturing, Scientific reports 10 (2020) 1–9.

[44] N. Fujita, H.-K. D.H.Bhadeshia, Modelling precipitation of niobium carbide in austenite: multicomponent diffusion, capillarity,and coarsening, Materials Science and Technology 17 (2001) 403–408.

[45] E. H. Sabzi, N.-T. Aboulkhair, X. Liang, X. Li, M. Simonelli, H. Fu, P. E. Rivera-Diaz-del Castillo, Grain refinement in laser powder bed fusion: The influence of dynamic recrystallization and recovery, Materials and Design 196 (2020) 109181.

[46] H. Sieurin, J. Zander, R. Sandstrom, Modelling solid solution hardening in stainless steels, Materials Science and Engineering A 415 (2006) 66–71.

[47] F. Abe, M. Murata, H. Miyazaki, Effect of tic and nbc carbides on creep life of stainless steels, Materials at High Temperatures 36 (2019) 37–45.

[48] R. Sandstrom, M. Farooq, B. Ivarsson, Influence of particle formation during long time ageing on mechanical properties in the austenitic stainless steel 310, Materials at High Temperatures 29 (2012) 1–7.

[49] X. Bai, J. Pan, G. Chen, L. J., W. J., Z. T., T. W., Effect of high temperature aging on microstructure and mechanical properties of hr3c heat resistant steel, Materials Science and Technology 30 (2014) 205–210.

[50] S. N. Dryepondt, J. Lehmusto, B. A. Pint, Effect of annealing and supercritical co2 exposure at 750c on the tensile properties of stainless steel and ni-based structural alloys, Materials and Corrosion (2021) 1–16.